

# Oriented Growth of ZnO Crystals on Self-Assembled Monolayers of Functionalized Alkyl Silanes

R. Turgeman,<sup>†</sup> O. Gershevit,<sup>†</sup> O. Palchik,<sup>†</sup> M. Deutsch,<sup>‡</sup> B. M. Ocko,<sup>#</sup>  
A. Gedanken,<sup>\*,†</sup> and C. N. Sukenik<sup>\*,†</sup>

*Departments of Chemistry and Physics, Bar-Ilan University, Ramat-Gan - 52900, Israel,  
and Physics Department, Brookhaven National Laboratory, Upton, New York 11973 USA*

*Received June 10, 2003; Revised Manuscript Received August 27, 2003*

**ABSTRACT:** Highly ordered ZnO crystals of 0.15  $\mu\text{m}$  width and 0.5  $\mu\text{m}$  length were grown on silicon wafers coated with a monolayer of  $\text{SiCl}_3(\text{CH}_2)_{11}-\text{O}-\text{C}_6\text{H}_5$  molecules. Various techniques (contact angle measurements, ellipsometry, ATR-FTIR) were employed for determining the quality of the monolayer coating. In addition, the bare and silane-coated Si wafers were studied by X-ray reflectivity (XR) and grazing-incidence diffraction (GID) using synchrotron radiation. The results obtained point to a possible relationship between the organization of the self-assembled monolayer (SAM) coating, the dipole moment of the headgroup, and the orientation of the ZnO crystals.

## 1. Introduction

Wide band gap materials have come to the forefront of scientific research because of an increasing need for the short wavelength photonic devices that are the future of optoelectronic technology. One of the important wide band gap materials is ZnO (3.3 eV at 300 K). It is a low cost II–VI semiconductor, which is environmentally friendly and has superior electronic and optical properties. It is more resistant to radiation damage than other common semiconductor materials such as Si, GaAs, CdS, and GaN, and thus should be useful for space applications.<sup>1</sup> ZnO is currently in use or being considered for use in electrooptical devices,<sup>2–8</sup> as a piezoelectric transducer,<sup>1,9,10</sup> varistor,<sup>1,11,12</sup> phosphor,<sup>1</sup> UV and microwave absorber,<sup>1,10</sup> and gas sensor,<sup>1,13–15</sup> and to make transparent conducting films.<sup>1,16</sup>

The physical properties of crystalline materials depend on their crystal morphology and habit, crystallite size, the content of impurities or dopants, and the presence of structural defects. For instance, measurements of cathode-luminescence and scanning tunneling spectroscopy of ZnO single crystals show that both surface electrical properties and luminescent characteristics depend on the face studied.<sup>17</sup> Polar O-terminated surfaces show an intrinsic conduction behavior with a surface band gap ranging from 0.4 to 0.8 eV. Zn terminated surfaces show mainly n-type conduction. The nonpolar faces present either intrinsic or p-type behavior.<sup>17</sup>

ZnO can be grown using a variety of techniques including vapor-phase transport,<sup>18,19</sup> sol–gel methods,<sup>19,20</sup> hydrothermal growth,<sup>21,22</sup> melt growth,<sup>23</sup> chemical vapor deposition (MOCVD),<sup>24</sup> electrochemical deposition,<sup>25–28</sup> laser ablation,<sup>29</sup> sputtering,<sup>30</sup> molecular beam epitaxy,<sup>31,32</sup> and spraying arc-discharge.<sup>33</sup> All these methods yield high quality ZnO and afford control over the orientation of the crystal grown and its exposed face, and, therefore, over its physical properties.

However, large-scale use will require the development of simple, low-cost approaches. One such method is to grow ZnO from aqueous solution at temperatures below 100 °C. The feasibility of ZnO crystal engineering under mild conditions was demonstrated by using surfactants<sup>34–36</sup> or polymers.<sup>37,38</sup>

One of the interesting techniques is growing ZnO on diblock copolymers.<sup>37,38</sup> These polymers are designed as molecular tools, such that one block (“anchor block”) interacts strongly with the mineral surface, whereas the other block (“solution block”) simply keeps the construction site in solution. The block, which interacts with the mineral, is hydrophilic, and the other block is hydrophobic. It was also found that diblock copolymers could play an important role in determining the morphology of  $\text{CaCO}_3$ <sup>39,40</sup> and  $\text{BaSO}_4$ <sup>41</sup> crystals.

The idea behind this approach is a mimicking of natural processes.<sup>38,42</sup> In natural processes surfactant-like peptides and glycopeptides interact with nuclei and growing crystals.<sup>43</sup> This interaction is achieved by a combination of two factors. One factor is related to the chemical functional group, and another is related to the structure, shape, orientation, and organization of the surfactants.

In accordance with this idea, crystal engineering has been done on SAM and Langmuir–Blodgett (LB) monolayers.<sup>44</sup> The literature has reported on  $\text{CaCO}_3$  crystals grown on functionalized alkanthiols, which were coated as self-assembled monolayers on a surface.<sup>45</sup> Growth of  $\text{CaCO}_3$  film under a Langmuir monolayer was also reported.<sup>46</sup> Self-assembly of alkyl silane mono- and multilayers on silicon has been studied recently in detail.<sup>47</sup> There is one report of the crystallization of ZnO thin films on a SAM surface.<sup>48</sup> This work, however, did not address the issue of crystal structure and orientation that are the subject of our work. Furthermore, there is one report about growing ZnO on various uncoated surfaces such as glass, Si wafers, ITO, etc. by Vayssieres and co-workers.<sup>49</sup> They reported that the type and crystallinity of the substrates had almost no influence on the crystal growth and orientation of ZnO micro-rod array. Other investigations of crystal engineering by SAM and LB monolayers have shown that the factors

\* Corresponding author. Aharon Gedanken Tel: 972–5318315.  
Fax: 972–5311250. E-mail: gedanken@mail.biu.ac.il.

<sup>†</sup> Department of Chemistry, Bar-Ilan University.

<sup>‡</sup> Department of Physics, Bar-Ilan University.

<sup>#</sup> Brookhaven National Laboratory.

influencing the crystal's morphology are the organization and the order of the monolayers on the surface and the structure of the crystal planes. There is little or no evidence for influencing crystal orientation by the chemical nature of the surface functional group.<sup>44,45</sup>

The challenge of the current research is to grow ZnO crystals on different surfaces and to understand the influence of the surface in determining the shape and the dimensions of the ZnO crystals. We have assembled siloxane monolayers on Si wafers. The anchor compound is an organo-trichlorosilane with a terminal phenyl ether; both the 11-carbon version ( $\text{SiCl}_3(\text{CH}_2)_{11}\text{O}-\text{C}_6\text{H}_5$ ) and the corresponding 3-carbon version were investigated and were compared to a silane with a simple alkyl chain (octadecyltrichlorosilane, OTS). The synthetic method used to grow the ZnO crystals is hydrolysis of a zinc nitrate solution.

The current study is aimed at understanding the influence of SAMs on ZnO crystal growth. We have conducted X-ray reflectivity (XR) and grazing incidence X-ray diffraction (GIXD) studies to probe the relationship between the organization of the SAM and the growth of the specific crystal face.

## 2. Experimental Section

**(a) Surface Treatment and Molecular Assembly.** Silicon wafers (n-type, P-doped, (100), 2–4  $\Omega\text{-cm}$ , Okmetic-Finland) were rinsed in chloroform, acetone, and ethanol for 30 s each and dried in a filtered  $\text{N}_2$  flow. Samples were then immersed in piranha solution (70:30 concentrated  $\text{H}_2\text{SO}_4\text{:H}_2\text{O}_2$  (30% v/v)) at 80 °C for 20 min. Samples were then washed 3 times with deionized water and dried in a filtered nitrogen stream.

Freshly cleaned samples of the silicon wafers were immersed in a solution of  $\text{SiCl}_3(\text{CH}_2)_{11}\text{O}-\text{C}_6\text{H}_5$  in dicyclohexyl 1/200 (v/v) under  $\text{N}_2$  for 2 h, keeping the temperature around 24 °C and the relative humidity at 30%. Samples were then taken out of the solution and cleaned. The cleaning involved sonication in chloroform, often followed by additional rinsing in chloroform. The samples were then dried with a filtered nitrogen stream.

**(b) Monolayer Characterization Methods. (1) Contact Angle and Ellipsometry.** Advancing and receding contact angle measurements of the coated silicon wafers were conducted under ambient conditions using a Rame-Hart NRL goniometer. All samples were measured at least three times. The film thickness on the Si wafers was measured by a spectrometric ellipsometer model M44 (J.A. WOOLLAM Co.) using 44 wavelengths between 680 and 1108 nm. Analysis employed the VASE software provided with the ellipsometer. The ellipsometrically determined thickness was compared to a theoretical thickness value estimated from the length of the fully extended chain of the SAM forming molecule, calculated using PCMODEL (Serena Software).

**(2) IR Spectroscopy.** ATR-FTIR was obtained on a Bruker Vector 22 spectrometer. Spectra of the as deposited films were collected using a  $60 \times 20 \times 0.45$  mm Si parallelogram prism, prepared in-house by polishing the two short edges of a freshly cut double-side polished silicon wafer to a 45° angle. The background data were collected after the piranha treatment of the cleaned ATR prism, and the sample data were collected after the deposition of the monolayer. The background spectrum of the clean ATR prism was subtracted from each sample spectra. Typically, 44 sample scans were collected, at a nominal resolution of  $4\text{ cm}^{-1}$ .

**(3) Surface-Specific X-ray Methods.** The bare and silane-coated Si wafers were studied by XR and grazing-incidence diffraction (GID), using synchrotron radiation. The crystallinity and orientation of the ZnO layers grown on these substrates were determined by using conventional X-ray diffraction at a laboratory-based source.

Since the XR and GID methods are well documented in the literature,<sup>50–54</sup> only a brief description of these techniques is presented here. An X-ray beam of wavelength  $\lambda$  impinging on an interface at an angle  $\alpha$  is partly reflected from, and partly refracted into, the interface. The fraction of the intensity reflected depends on the surface-normal density profile, and is given to a very good approximation by the “master equation”:

$$R(q_z)/R_F(q_z) = \left| \frac{1}{\rho_\infty} \int_{-\infty}^{\infty} \frac{d\langle\rho(z)\rangle}{dz} e^{iq_z z} dz \right|^2 \quad (1)$$

where  $q_z = (4\pi/\lambda) \sin \alpha$  is the surface-normal momentum transfer, and  $\rho_\infty$  is the bulk electron density. The axis  $z$  is chosen to denote the surface normal direction, and  $d\langle\rho(z)\rangle/dz$  is the derivative of electron density profile averaged in the surface-parallel directions ( $x, y$ ) over the coherence length of the X-rays. The right-hand side of eq 1 is the standard crystallographic structure factor of the interface.  $R_F(q_z)$  is the Fresnel reflectivity curve from an ideally flat and abrupt interface, having a profile  $\rho(z)$  given by a step function. It is given by

$$R_F(q_z) = |(q_z - \sqrt{q_z^2 - q_c^2})/(q_z + \sqrt{q_z^2 - q_c^2})|^2 \quad (2)$$

where  $q_c$  is the critical momentum transfer for total external reflection, of order  $0.03\text{ Å}^{-1}$  for our samples.  $\langle\rho(z)\rangle$  in eq 1 is usually determined by modeling the surface density profile by a series of slabs, each characterized by a single density, thickness, and surface roughness, calculating the right-hand side of eq 1 analytically, and then fitting the resultant expression to the measured  $R(q_z)$ . This yields the parameters determining the density profiles.

For an angle of incidence below the critical angle for total external reflection of the X-ray beam impinging on the surface,  $\leq 0.2\text{--}0.3^\circ$ , the refracted beam becomes evanescent, penetrates only about 50 Å below the surface, and travels parallel to the surface. If the molecules are ordered parallel to the surface, the evanescent wave will be diffracted to produce Bragg peaks in particular directions. Diffraction from a 3D crystal occurs when Bragg law is satisfied. Namely, the scattering vector  $\mathbf{q}$  coincides with the reciprocal lattice vector  $2\pi(h\mathbf{a}^* + k\mathbf{b}^* + l\mathbf{c}^*)$ , where  $\mathbf{a}^*$ ,  $\mathbf{b}^*$ ,  $\mathbf{c}^*$  are the reciprocal lattice vectors of the unit cell axes.  $h$ ,  $k$ ,  $l$  are integers that represent the Miller indices of the Bragg-diffracting plane. For a 2D crystal, such as may exist at the surface, the selection rules refer to the scattering vector's surface-parallel component  $q_{||}$ .

Several important observables can be extracted from the measured diffraction pattern. The angular position,  $2\theta$ , of the Bragg peak yields the repeat distance  $d = 2\pi/q_{||}$  for the 2-D lattice structure, where  $q_{||} = (4\pi/\lambda)\sin(2\theta/2)$ . Indexing the peaks in the pattern yields their 2D unit cell vectors  $\mathbf{a}$ ,  $\mathbf{b}$ . The full-width at the half-maximum (fwhm),  $\Delta q_{||}$ , of an  $(h, k)$  Bragg diffraction peak yields, through the 2D equivalent of the Debye–Scherrer equation,  $L = (0.9 \times 2\pi)/\Delta q_{||}$ , the crystalline coherence length  $L$  within the monolayer plane, in the direction associated with the  $(h, k)$  “planes”. Further details on the surface-specific X-ray techniques above can be found in refs 50–54.

The synchrotron X-ray measurements were carried out using a conventional 6-circle diffractometer at beamline X22A, National Synchrotron Light Source, Brookhaven National Laboratory, at a wavelength of  $\lambda = 1.155\text{ Å}$ . The samples were placed in a sealed cell, having Kapton X-ray windows. A flow of oxygen-free helium through the cell reduced parasitic scattering and minimized beam damage to the sample.

**(c) Crystallization.** Figure 2 explains the experimental setup used for the crystallization process. The coated silicon wafers were inserted into a Teflon holder. The Teflon holder was put inside the supersaturated solution on a glass ring with the wafer's coated surface facing downward to avoid ZnO crystals aggregating adventitiously on the surface. To minimize the effects of local variations in temperature, supersaturation, pH value, and the stirring, several wafers were coated simultaneously.

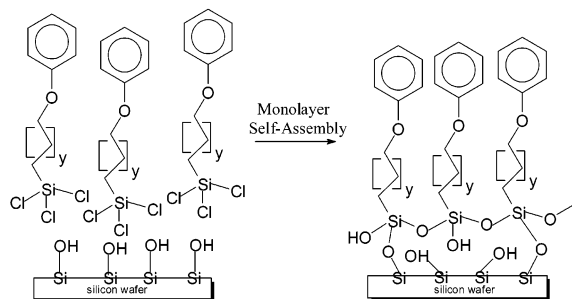


**Figure 1.** The self-assembly process.  $\text{SiCl}_3(\text{CH}_2)_{11}-\text{O}-\text{C}_6\text{H}_5$  molecules adsorb to the surface via hydrolysis of Si-Cl bonds.

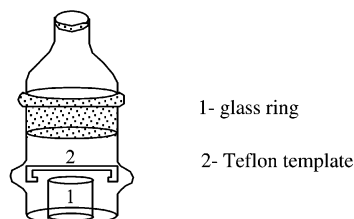


**Figure 2.** The experimental setup of the crystallization process. The vessel is sealed by a rubber septum to achieve stable conditions of concentration and temperature.

Aqueous solutions of zinc nitrate ( $\text{Zn}(\text{NO}_3)_2 \cdot 6\text{H}_2\text{O}$ , Aldrich) and hexamethylene tetramine (Aldrich, HMT) were mixed at room temperature. Under these conditions, no ZnO is formed. The final concentrations of  $\text{Zn}^{2+}$  and HMT were 0.03 mol/L. Crystal growth experiments were conducted in a water-jacketed cell of 100 mL capacity at temperature of 95 °C. A magnetic stirrer was used to agitate the solution gently. The high temperature was chosen to prevent the formation of zinc hydroxide, and afford the decomposition of HMT to ammonia and formaldehyde. This causes a shift of the pH of the solution from 5 to around 6, which is enough to exceed the solubility product of ZnO. We stopped the crystallization after 90 min by cooling the vessel to room temperature. After the crystallization process, the ZnO-coated wafers were washed with distilled water and then with ethanol several times, and then dried with stream of purified nitrogen.

**(d) Crystals Characterization Methods.** The crystals were characterized by scanning electron microscope (SEM) measurements (JEOL-JSM 840, scanning electron microscope), high resolution-SEM (HR-SEM) (LEO Gemini), 982 field emission gun SEM (FEG-SEM) operating at 4 kV accelerating voltage, and X-ray powder diffraction (Bruker AXS D\* Advance Powder X-ray diffractometer, using  $\text{Cu K}\alpha = 1.5418 \text{ \AA}$  radiation). The SEM pictures were analyzed in the following way. In each picture, we counted the total number of ZnO crystals as well as the number of crystals with a perpendicular orientation. The results were presented as percentage of oriented crystals out of the total number of ZnO crystals. Samples exhibiting more than 50% oriented crystals are considered as showing oriented growth.

### 3. Results and Discussion

**(a) Monolayer Characterization.** Various techniques were used to check monolayer quality. The thickness of the monolayers was measured by using ellipsometry and by XR measurements. A comparison of the two results with the theoretical thickness (Si atom to para-H) shows good agreement as shown in Table 1.

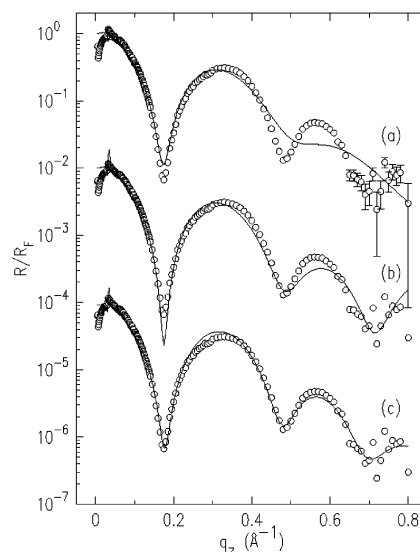


**Figure 3.** The measured and Fresnel-divided X-ray reflectivity (open circles) of the Si wafer coated by a monolayer of  $\text{SiCl}_3(\text{CH}_2)_{11}-\text{O}-\text{C}_6\text{H}_5$  whose measured thickness was 1.55 nm, with fits (lines) to (a) 1-slab, (b) 2-slab, and (c) 3-slab models. The corresponding density profiles are given in Figure 4. Curves are shifted by two decades each for clarity.

We characterized the structures of the phenyl-terminated SAMs through FTIR-ATR measurements. In this spectrum, the symmetric methylene stretch ( $\nu_s\text{CH}_2$ ) appears at  $2852 \text{ cm}^{-1}$ , the antisymmetric methylene stretch ( $\nu_a\text{CH}_2$ ) appears at  $2921 \text{ cm}^{-1}$ , and the C-H stretches associated with the terminal phenyl groups appear above  $3000 \text{ cm}^{-1}$ . Previous studies have shown that the position of the  $\nu_a\text{CH}_2$  band is sensitive to the degree of conformational order (or crystallinity) of organic thin films.<sup>55</sup> We find that when alkyl chains are substituted with planar phenyl groups, the  $\nu_a\text{CH}_2$  bands appear at higher wavelengths than those of a well-order SAM comprised of only alkyl chains having similar molecular length.<sup>56</sup>

Polarized IR measurements give the dichroic ratio between the surface-perpendicular IR beam to the surface-parallel beam.<sup>57,58</sup> This ratio can give information about the tilt angle of the molecules makes with the surface normal. These measurements show that the tilt angle of the monolayers is  $24^\circ$ . This result explains why the XR and ellipsometrically measured layer thickness is smaller than the theoretical length of an extended molecule.

The small hysteresis value,  $4^\circ$ , in the CA measurements implies that an homogeneous coating of the silicon surface is obtained. The corresponding hysteresis value for silicon wafers homogeneously coated with octadecyltrichlorosilane (OTS) is  $3^\circ$ .<sup>59</sup> Thus, it is assumed that a full coverage of the surface by monolayers of  $\text{SiCl}_3(\text{CH}_2)_{11}-\text{O}-\text{C}_6\text{H}_5$  is achieved.

The measured XR from a wafer coated by a monolayer of  $\text{SiCl}_3(\text{CH}_2)_{11}-\text{O}-\text{C}_6\text{H}_5$ , divided by the Fresnel reflectivity  $R_F$ , is shown in Figure 3. The sharp, well-defined Kiessig fringes observed indicate that the monolayer is

**Table 1.** Summary of the Properties of the Surface Derived from All the Characterization Tools

thickness of layer (Å)			wetting properties, CA adv/rec/hyst	film crystallinity $\text{CH}_{2\text{antisym}}/\text{CH}_{2\text{sym}}, \text{ cm}^{-1}$	tilt angle		roughness (Å)
theoret	ellipsom	XR			IR	XR	
20.6	$19.4 \pm 2$	$18.4 \pm 0.4$	$90^\circ/86^\circ/4^\circ$	2921/2852	$24^\circ$	$13^\circ \pm 6^\circ$	$3.7 \pm 0.6$



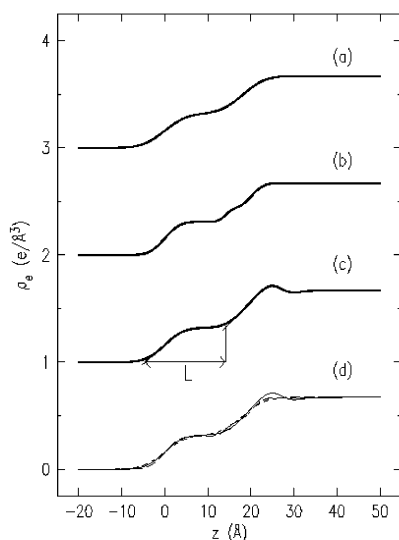


**Figure 4.** The real space surface-normal electron density (solid lines), as derived from the fits in Figure 3, to the (a) 1-slab, (b) 2-slab, and (c) 3-slab models. (d) Overlap of all three density profiles showing their close similarity. Curves are shifted by  $\rho_e = 1 \text{ e}/\text{\AA}^3$  each for clarity.

densely packed and uniform, both microscopically and macroscopically. As pointed out in the very detailed study of Tidswell et al.,<sup>60</sup> the first sharp minimum results from destructive interference between waves reflected from the upper and lower surfaces of the organic layer. Its position,  $q_z^m$ , is related to the layer's thickness,  $L$ , by  $L\sqrt{(q_z^m)^2 - (q_c)^2} = \pi$ . With a measured  $q_c \approx 0.03 \text{ \AA}^{-1}$ , this yields  $L \approx 18.3 \text{ \AA}$ . As we show below, this value is within  $\leq 1 \text{ \AA}$  of the results obtained from both a more sophisticated model-based analysis of the reflectivity, and theoretical model calculations for the length of the alkyl-phenyl chain.

The fact that the positions of the higher  $q_z$  minima in the reflectivity curve are not integer multiples of  $q_z^m$  indicates that there is additional structure within the film. Previous studies show that the extraction of this internal structure from a limited  $q_z$  range reflectivity curve, such as ours, is neither straightforward nor unambiguous. We have therefore followed Tidswell et al., and carried out fits to slab models having an increasing number of slabs, from 1 to 4, which allow an increasing amount of detail and flexibility, albeit at the unavoidable cost of an increasing number of fit parameters. The slab models for  $\langle \rho(z) \rangle$  included a density and width for each slab, and employed eq 1 to calculate the reflectivity. For each interface between slabs a finite interface width parameter, representing the interfacial roughness, was also included in the fit. The best fits to the measured  $R/R_F$  curve are shown in solid lines in Figure 3, and the corresponding density profiles, obtained from the best-fit parameters, are plotted in solid lines in Figure 4.

The most outstanding feature of the four  $\rho(z)$  curves is the fact that they are almost identical in shape, as shown in Figure 4d, indicating that the fits have captured well the main features of the density profile. This agrees well with the conclusion of the detailed study of Tidswell et al.<sup>60</sup> that even though a unique identification of a particular part of the molecule, e.g., the phenyl, the alkyl, or the headgroup, may not be

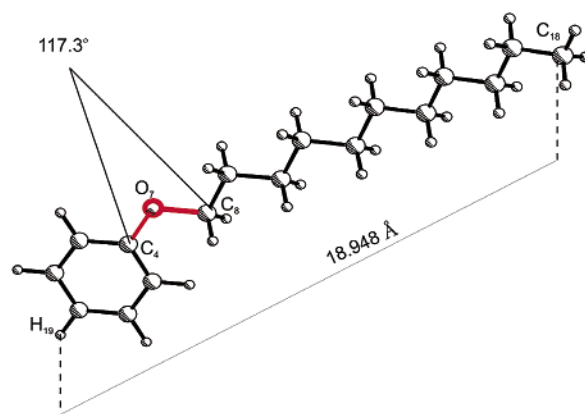


**Figure 5.** The molecular conformation as obtained from theoretical configurational energy calculations. The distance between C18-H19 is 18.948 Å and angle C4-O7-C8 is 117.3°.

always possible, the density profile is almost uniquely determined by the fit despite the different models. This said, it should be noted that some features in the density profile are clearly identifiable. The leftmost plateau in the profiles can be confidently associated with the alkyl plus phenyl tail of the molecules. Thus, following the method of Tidswell et al., we used the graphical construction shown in Figure 4d to extract the thickness, marked by the arrow  $L$ , of the slab corresponding to the molecule's tail, directly from the actual density profile. We obtain thicknesses ranging from  $L = 18.2 \text{ \AA}$  (for the 1-slab model) to  $L = 19.1 \text{ \AA}$  (for the 3-slab model). The average of these values,  $L = 18.4 \pm 0.4 \text{ \AA}$ , can be considered therefore as a reasonable estimate for the thickness of the slab representing the tail of the molecule. This value agrees well with the 18.3 Å derived above from the position of the first minimum of  $R(q_z)$ .

Calculations using PC model (Serena Software) yield the molecular conformation shown in Figure 5, where the planes of the alkyl and phenyl moieties coincide, and the C-O-C bonds form an angle very close to that of a C-C-C bond. The tail length obtained from the calculation in this fully extended configuration is 18.9 Å, close to the value derived above from the model fits. This leads to two conclusions. First, the plane of the phenyl ring coincides with that of the alkyl chain, which is tilted by only a small angle from the surface normal. This renders the possibility of the phenyl ring serving as a template for *surface-normal* epitaxial growth of ZnO in the (001) direction highly unlikely, since this would require the ring to be oriented surface parallel. Second, the values above are consistent with a small molecular tilt of  $\cos^{-1}[(18.4 \pm 0.4)/18.9] \approx (13 \pm 6)^\circ$  from the surface normal. This is lower than, but well within two standard deviations, from the IR-derived value discussed above.

The normalized GID pattern measured for the same monolayer-coated Si wafer is shown in Figure 6. The single peak at  $q_{||} = 1.41 \text{ \AA}^{-1}$  indicates an hexagonal packing with a lattice spacing  $d = 2\pi/1.41 = 4.46 \text{ \AA}$ ,  $\sim 8\%$  larger than the 4.77 Å of the hexagonally packed rotator phase of alkanes. The area/molecule in the molecular-axis plane is correspondingly larger:  $21.3 \text{ \AA}^2/\text{molecule}$  (assuming a molecular tilt of  $13^\circ$ ) as compared to  $19.7 \text{ \AA}^2/\text{molecule}$ . The larger molecular area is not surprising, in view of the bulkier phenyl terminal group.

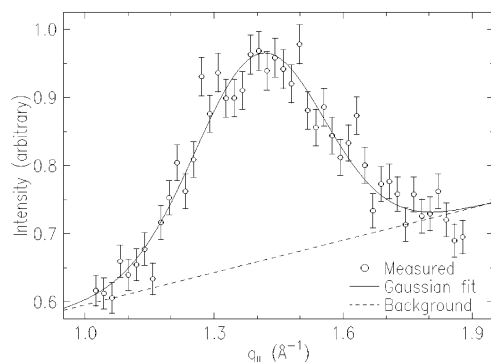


**Figure 6.** The grazing incidence diffraction pattern (open circles) and its fit by a Gaussian (solid line) plus a linear background (dashed line) for the monolayer-coated silicon. The single peak position at  $1.41 \text{ \AA}^{-1}$ , indicates hexagonal packing, with a nearest-neighbor distance of  $5.15 \text{ \AA}$ . The peak width of  $0.15 \text{ \AA}^{-1}$  indicates short-range in-plane order only, with an order coherence length of  $\sim 40 \text{ \AA}$ .

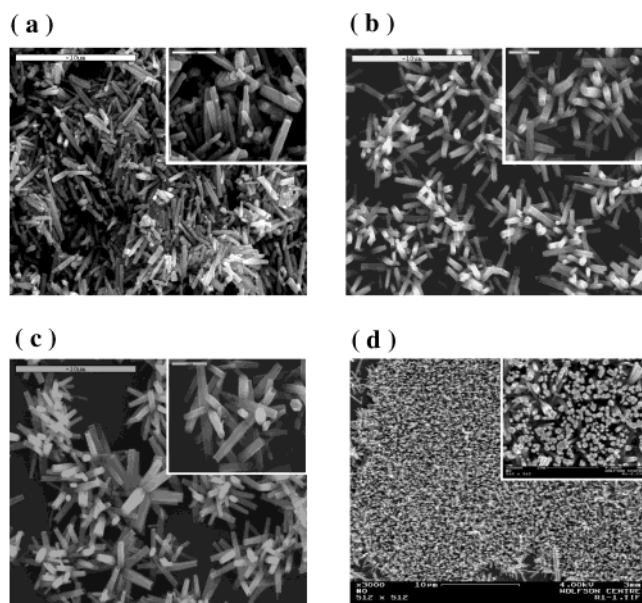


**Figure 7.** SEM pictures of (a) standard ZnO grown from a saturated solution; (b) ZnO grown on bare silicon; (c) ZnO grown on silicon wafer covered by silane monolayers whose thickness is  $1.75 \text{ nm}$ ; (d) HR-SEM picture of ZnO grown on a silicon wafers covered by a silane monolayer whose thickness is  $1.55 \text{ nm}$ .

The bulky phenyl moiety should also inhibit close packing of the alkyl chains at their smaller area/molecule. The packing frustration due to the different cross sections of the alkyl chain and phenyl moieties is, most likely, the reason for the very small surface-parallel crystalline coherence length,  $\lambda = (0.9 \times 2\pi) / \Delta q_{\parallel} \approx 40 \text{ \AA}$ , obtained from the Debye-Scherrer formula using the  $\Delta q_{\parallel} \approx 0.15 \text{ \AA}^{-1}$  width of the measured GID peak.

**(b) Crystals Characterization.** Figure 7 compares the morphology of ZnO crystals grown from the bulk solution (a), those grown on bare silicon (b), and those grown on silicon wafers coated with  $\text{SiCl}_3(\text{CH}_2)_{11}\text{O}-\text{C}_6\text{H}_5$  (c) and (d). The difference between Figure 7, panels c and d, is the thickness of the silane monolayers. The best orientation of the ZnO crystals is observed in Figure 7d, where all the crystals are perpendicular to

**Table 2.** Observed Percentage of Oriented Crystals as a Function of Surface Properties

sample	thickness (nm) ellipsometer	CA (degrees) adv/rec/hysteresis	percentage of crystals oriented (002) (%)
(1) C <sub>11</sub>	1.42	84/75/9	52
(2) C <sub>11</sub>	1.47	84/76/8	56.3
(3) C <sub>11</sub>	1.47	85/73/12	64
(4) C <sub>11</sub>	1.52	89/81/8	100
(5) C <sub>11</sub>	1.55	89/80/9	100
(6) C <sub>11</sub>	1.55	93/88/5	30
(7) C <sub>11</sub>	1.73	93/88/5	10
(8) C <sub>11</sub>	1.75	90/85/5	0
(9) C <sub>11</sub>	1.83	94/90/4	18
(10) C <sub>11</sub>	1.84	95/85/10	30
(11) C <sub>11</sub>	1.90	97/88/9	18.5
(12) C <sub>11</sub>	2.00	95/90/5	0
(13) C <sub>11</sub>	2.03	97/91/6	0
(14) C <sub>3</sub>	0.87	85/75/10	26
(15) C <sub>3</sub>	1.08	82/72/10	25.2
(16) C <sub>3</sub>	0.99	83/74/9	23.8
(17) C <sub>3</sub>	0.96	84/76/8	22.5
(18) bare Si			16.2

the silicon surfaces. All other pictures show less well-oriented crystal arrangements. The bare silicon surface, Figure 7b, reveals a partial arrangement of the ZnO facing the reader, while the other crystals are found tilted at various angles to the surface. The same is true for Figure 7c, where the underlying monolayer had a thickness of  $1.75 \text{ nm}$ . Given that both of these thicknesses are less than or equal to what is expected for a surface covered with an optimally packed SAM of the C<sub>11</sub> phenyl ether, this difference will be further discussed below.

All the ZnO crystals are well-shaped, monodispersed, and hexagonal with clear face boundaries. The width of the crystals decrease in the following order  $7a > 7b > 7c > 7d$ . Thus, the best orientated crystals also have the smallest width. The width of the crystals in Figure 7a is  $0.5 \text{ \mu m}$ , while those in Figure 7d have a width of  $0.15 \text{ \mu m}$ . The length of the crystals is also changing, and the longest crystals ( $3 \text{ \mu m}$ ) are grown from the solution. The shortest are observed in Figure 7d where  $0.5 \text{ \mu m}$  long ZnO crystals are detected.

Attempts have been also made to grow ZnO crystals on a monolayer made from  $\text{SiCl}_3(\text{CH}_2)_3\text{O}-\text{C}_6\text{H}_5$  (C<sub>3</sub>). The crystal growth process is identical to that used on monolayer films made from  $\text{SiCl}_3(\text{CH}_2)_{11}\text{O}-\text{C}_6\text{H}_5$  (C<sub>11</sub>). The SEM picture obtained for the ZnO crystals resembles more that of Figure 7b,c than that of Figure 7d. This provides additional support for the importance of a substrate layer with some measure of organization in determining the orientation of the ZnO crystals.

In Table 2 we summarize the percentages of oriented crystals found on each of our various surfaces, along with the thickness and contact angle data for that particular organic thin film. The results of ZnO growth on  $\text{SiCl}_3(\text{CH}_2)_{11}\text{O}-\text{C}_6\text{H}_5$  (C<sub>11</sub>) monolayers can be divided into two groups. The ZnO grown on layers whose thickness is  $1.48 \pm 0.07 \text{ nm}$ , and the ZnO grown on monolayers thicker than  $1.70 \text{ nm}$ . The first group reveals an oriented growth, with more than 50% of the crystals perpendicular to the silicon wafer (sample 6 is only 30% but within the overall trend), while for the second group an unoriented growth is observed. The second group includes those surfaces with lower contact angle hysteresis and with thicknesses closer to that of

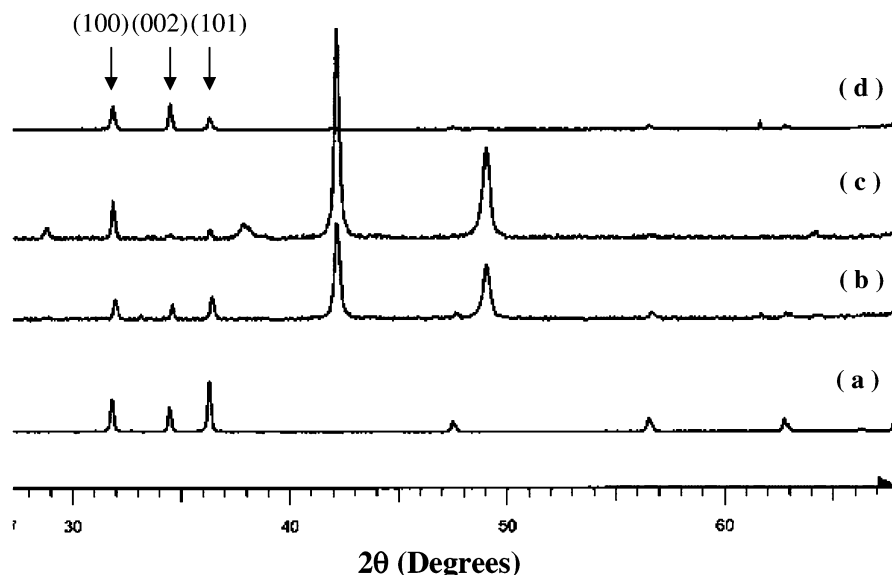


**Figure 8.** XRD patterns of (a) standard ZnO grown from a saturated solution; (b) ZnO grown on bare silicon; (c) ZnO grown on silicon wafer covered by silane monolayers whose thickness is 1.75 nm; (d) ZnO grown on a silicon wafers covered by a silane monolayer whose thickness is 1.55 nm. The first three diffraction peaks show that the ZnO has a Zincite phase.

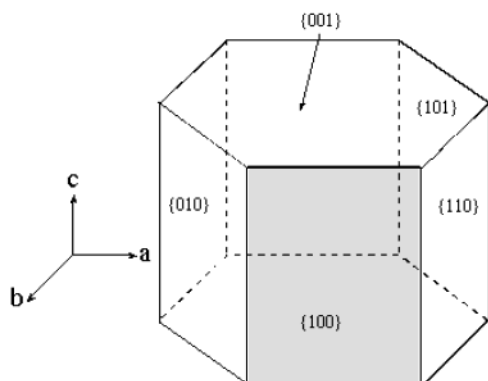


**Figure 9.** Schematic representation of the ZnO crystal.

a fully coated well-ordered surface. Further studies are now in progress to investigate those samples with monolayer thickness of 2.0 nm (0% of perpendicular crystals) which might show a parallel orientation of ZnO to the substrate.

The XRD diffraction patterns of the ZnO crystals are presented in Figure 8. We have kept the order of the presentation as in Figure 7, where Figure 8a depicts the solution results and Figure 8d depicts the ZnO grown on a monolayer whose thickness was 1.55 nm. ZnO is a polar crystal whose polar axis is the *c*-axis; its space group is  $C_{6v} = P6_3mc$ .<sup>61</sup> In the ZnO structure, each  $Zn^{2+}$  ion is surrounded by four  $O^{2-}$  ions and vice versa. The crystal structure of ZnO is like the wurtzite-structure, as shown in Figure 9.

Figure 8a,b represent unoriented growth, where the intensity ratio of the (100):(002):(101) matches the literature powder data.<sup>62</sup> Preferential growth is observed where the (100) (in Figure 8c) and (002) (in Figure 8d) appear as the most intense diffraction peaks. The intensity ratio in these figures clearly deviates from the literature data, pointing to a preferential growth of the crystals. The (002) being the most intense diffraction pattern in Figure 8d fits well the SEM picture, Figure 7d, demonstrating crystals whose (002) hexagonal plane

is parallel to the surface. The strong intensity of the (100) plane in Figure 8c is also in accordance with the length of the crystals in the corresponding Figure 7c whose length is 3 times larger than the crystals in Figure 7d.

The XR and GID measurements obtained for the  $SiCl_3(CH_2)_{11}-O-C_6H_5$  films are comparable to those for OTS, namely, that of an hexagonally organized monolayer. We suggest that the  $C_{11}$  phenyl-ether monolayers all share this basic arrangement, with varying degrees of perfection and flexibility. This varies from coating to coating and is reflected in differences in thickness and wetting properties.

Our understanding of the orientation of the crystal growth emphasizes the SEM results. Perpendicular, well-formed, organized ZnO crystals are obtained only for substrates where the thickness of the  $SiCl_3(CH_2)_{11}-O-C_6H_5$  monolayer was 1.4–1.6 nm. We do not see comparable organization of the ZnO crystals on (i) bare silicon wafers, (ii) OTS monolayers, (iii)  $SiCl_3(CH_2)_3-O-C_6H_5$ , and (iv) for  $SiCl_3(CH_2)_{11}-O-C_6H_5$  monolayers whose thickness was  $>1.7$  nm. The OTS and the fully covered  $SiCl_3(CH_2)_{11}-O-C_6H_5$  films exhibit comparable organization in the XR and GID measurements. While the organization of the film plays a role in oriented ZnO formation, well-organized OTS is not sufficient. We suggest that the mild molecular dipole (1–2 D) of the phenyl ether chromophore, when properly organized at the surface of the monolayer film, is crucial to the formation of oriented ZnO. This explains the difference between the ZnO growth on  $SiCl_3(CH_2)_{11}-O-C_6H_5$  and the OTS. Support for the argument that this dipolar unit influences the ZnO is that the plane of ZnO preferentially formed at the interface with the monolayer is the (001) plane of ZnO. This is a polar plane, in contrast to the (100), (010), (110), and the (101) planes, which are the nonpolar planes of ZnO.

The importance of the less than full monolayer coverage for oriented ZnO growth may lie in the flexibility needed for the aromatic ring to freely rotate and perhaps bend to accommodate the orientation of ZnO



on its outer surface. This freedom is restricted in a close-packed monolayer coating. Only if this mix of order and flexibility for the dipolar functional group is achieved are organized ZnO crystals obtained. Bare silicon lacks the substrate organization. OTS lacks the dipole moment. The short chain version of phenyl ether silane (C<sub>3</sub>) lacks the substrate organization, and the fully covered, more closely packed versions of the SiCl<sub>3</sub>-(CH<sub>2</sub>)<sub>11</sub>-O-C<sub>6</sub>H<sub>5</sub> monolayers (thickness > 1.7 nm) is less than optimal for oriented ZnO growth because of the hindered motion of the aromatic ring.

Having shown that monolayer covered surfaces can influence the orientation of ZnO crystal growth, as a function of their nature and organization, we are currently exploring the possibility of incorporating phenyl-ether groups bearing other functional groups at the exposed (para) position and examining how this additional parameter can be used to influence both monolayer packing and crystal growth.

**Acknowledgment.** The authors gratefully acknowledge support from the Germany-Israel Program (DIP) of the German DLR. Beamtime at X22A, NSLS, is gratefully acknowledged. Brookhaven National Laboratory is supported by the U. S. Department of Energy under contract DE-AC02-76CH00016.

### References

- Look, D. C. *Mater. Sci. Eng. B* **2001**, *80*, 383.
- Chopra, K. L.; Das, S. R., Eds. *Thin Film Solar Cells*; Plenum: New York, 1983.
- Karzel, H.; Potzel, W.; Kofferlein, M.; Schiessl, W.; Steiner, M.; Hiller, U.; Kalvius, G. M.; Mitchell, D. W.; Das, T. P.; Blaha, P.; Schwarz, K.; Pasternak, M. P. *Phys. Rev. B* **1996**, *53*, 11425.
- Cho, S.; Ma, J.; Kim, Y.; Sun, Y.; Wong, G. K. L.; Ketterson, J. B. *Appl. Phys. Lett.* **1999**, *75*, 2761.
- Kong, L. B.; Li, F.; Zhang, Y.; Yao, X. *J. Mater. Sci. Lett.* **1998**, *17*, 769.
- Shih, W. C.; Wu, M. S. *J. Cryst. Growth* **1994**, *137*, 319.
- Troy, C. T. *Photonics Spectra* **1997**, *31*, 34.
- Vanheusden, K.; Seager, C. H.; Warren, W. L.; Tallant, D. R.; Caruso, J.; Hampden Smith, M. J.; Kodas, T. T. *J. Lumin.* **1997**, *75*, 11.
- Bailar, J. C.; Emeleus, H. J.; Nyholm, R.; Trotman-Dickenson, A. F., Eds.; *Comprehensive Inorganic Chemistry*; Pergamon Press: Oxford, 1973.
- Hutson, A. R. *Phys. Rev. Lett.* **1960**, *4*, 505.
- Gupta, T. K. *J. Am. Ceram. Soc.* **1990**, *73*, 1817.
- Lee, J.; Hwang, J. H.; Mashek, J. J.; Mason, T. O.; Miller, A. E.; Siegel, R. W. *J. Mater. Res.* **1995**, *10*, 2295.
- Jin, Z. C.; Hamberg, I.; Granqvist, C. G.; Sernelius, B. E.; Berggren, K. F. *Thin Solid Films* **1988**, *164*, 381.
- Chatterjee, A. P.; Mitra, P.; Mukhopadhyay, A. K. *J. Mater. Sci.* **1999**, *34*, 4225.
- Seiyama, T.; Kato, A.; Fujiishi, K.; Nagatani, M. *Anal. Chem.* **1962**, *34*, 1502.
- Brett, M. J.; Parsons, R. R. *Solid State Commun.* **1985**, *54*, 603.
- Urbiet, A.; Fernandez, P.; Hardalov, C.; Piqueras, J.; Sekiguchi, T. *Mater. Sci. Eng. B* **2002**, *91–92*, 345.
- Look, D. C.; Reynolds, D. C.; Sizelove, J. R.; Jones, R. L.; Litton, C. W.; Cantwell, G.; Harsch, W. C. *Solid State Commun.* **1998**, *105*, 399.
- Takahashi, N.; Kaiya, K.; Omichi, K.; Nakamura, T.; Okamoto, S.; Yamamoto, H. *J. Cryst. Growth* **2000**, *209*, 822.
- Spanhel, L.; Anderson, M. A. *J. Am. Chem. Soc.* **1991**, *113*, 2826.
- Suscavage, M.; Harris, M.; Bliss, D.; Yip, P.; Wang, S. Q.; Schwall, D.; Bouthillette, L.; Bailey, J.; Callahan, M.; Look, D. C.; Reynolds, D. C.; Jones, R. L.; Litton, C. W. *MRS Internet J. Nitride Semicond. Res.* **1999**, *4*, G 3.40, Suppl. 1.
- Kortounova, E. V.; Lyutin, V. I. *Ann. Chim. Sci. Mat.* **1997**, *22*, 647.
- Nause, J. III—Vs Review **1999**, *12*, 4, 28.
- Kim, J. S.; Marzouk, H. A.; Reucroft, P. J.; Hamrin, C. E., Jr. *Thin Solid Films* **1992**, *217*, 133.
- Masanobu, I.; Takashi, O. *Appl. Phys. Lett.* **1996**, *68*, 2439.
- Peulon, S.; Lincot, D. *J. Electrochem. Soc.* **1998**, *145*, 864.
- Yoshida, T.; Tochimoto, M.; Schlettwein, D.; Wohrle, D.; Sugiyama, T.; Minoura, H. *Chem. Mater.* **1999**, *11*, 2657.
- O'Regan, B.; Schwartz, D. T.; Zakeeruddin, S. M.; Gratzel, M. *Adv. Mater.* **2000**, *12*, 1263.
- Ardakani, H. K. *Thin Solid Films* **1996**, *287*, 280.
- Valentini, A.; Quaranta, F.; Penza, M.; Rizzi, F. R. *J. Appl. Phys.* **1993**, *73*, 1143.
- Chen, Y. F.; Bagnall, D. M.; Koh, H. J.; Park, K. T.; Hiraga, K.; Zhu, Z. Q.; Yao, T. *J. Appl. Phys.* **1998**, *84*, 3912.
- Chen, Y. F.; Bagnall, D. M.; Zhu, Z. Q.; Sekiuchi, T.; Park, K. T.; Hiraga, K.; Yao, T.; Koyama, S.; Shen, M. Y.; Goto, T. *J. Cryst. Growth* **1997**, *181*, 165.
- Kitano, M.; Hamabe, T.; Maede, S. *J. Cryst. Growth* **1993**, *128*, 1099.
- Guo, L.; Ji, L. Y.; Xu, H. *J. Am. Chem. Soc.* **2002**, *124*, 14864.
- Tian, Z. R.; Voigt, J. A.; McKenzie, B.; McDermott, J. M. *J. Am. Chem. Soc.* **2002**, *124*, 12954.
- Choi, K. S.; Lichtenegger, H. C.; Stucky, G. D. *J. Am. Chem. Soc.* **2002**, *124*, 12402.
- Kumar, R. V.; Elgamiel, R.; Koltypin, Y.; Norwig, J.; Gedanken, A. *J. Cryst. Growth* **2003**, *250*, 409.
- Öner, M.; Norwig, J.; Meyer, W. H.; Wegner, G. *Chem. Mater.* **1998**, *10*, 460.
- Marentette, J. M.; Norwig, J.; Stöckelmann, E.; Meyer, W. H.; Wegner, G. *Adv. Mater.* **1997**, *9*, 647.
- Colfen, H.; Antonietti, M. *Langmuir* **1998**, *14*, 582.
- Limin, Q.; Colfen, H.; Antonietti, M. *Chem. Mater.* **2000**, *12*, 2392.
- Seldak, M.; Antonietti, M.; Colfen, H. *Macromol. Chem. Phys.* **1998**, *199*, 247.
- Nancollas, G. H., Ed.; *Dahlem Workshop on Biological Mineralization and Demineralization*; Springer-Verlag: Berlin, 1982.
- Kuzemenko, I.; Rapaport, H.; Kajaer, K.; Als-Nielsen, J.; Weissbuch, I.; Lahav, M.; Leiserowitz, L. *Chem. Rev.* **2001**, *101*, 1659.
- Aizenberg, J.; Black, A. J.; Whiteside, G. M. *J. Am. Chem. Soc.* **1999**, *121*, 4500.
- DiMasi, E.; Patel, V. M.; Sivakumar, M.; Olszta, G. M.; Yang, Y. P.; Gower, L. B. *Langmuir* **2002**, *18*, 8902.
- Baptiste, A.; Gibaud, A.; Bardeau, J. F.; Wen, K.; Maoz, R.; Sagiv, J.; Ocko, B. M. *Langmuir* **2002**, *18*, 3916.
- De Guire, M. R.; Niesen, T. P.; Supothina, S.; Wolff, J.; Bill, J.; Sukanik, C. N.; Aldinger, F.; Heuer, A. H.; Ruhle, M. *Z. Metallkd.* **1998**, *89*, 758.
- Vayssieres, L.; Keis, K.; Lindquist, S.-E.; Hagfeldt, A. *J. Phys. Chem. B* **2001**, *105*, 3350.
- Deutsch, M.; Ocko, B. M. *Encyclopedia of Applied Physics*; Trigg, G. L., Ed.; VCH: New York, 1998; Vol. 23, p 479.
- Daillant, J.; Gibaud, A., Eds. *X-ray and Neutron Reflectivity: Principles and Applications*; Springer: Berlin, 1999.
- Als-Nielsen, J.; Jacquemain, D.; Kjaer, K.; Leveiller, F.; Lahav, M.; Leiserowitz, L. *Phys. Rep.* **1994**, *246*, 252.
- Daillant, J.; Alba, M. *Rep. Prog. Phys.* **2002**, *63*, 1725.
- Als-Nielsen, J.; McMorrow, D. *Elements of Modern X-ray Physics*; Wiley: New York, 2001.
- Lee, S.; Puck, A.; Graupe, M.; Colorado, R.; Shon, Y. S.; Lee, T. R.; Perry, S. S. *Langmuir* **2001**, *17*, 7364.
- Gershevit, O.; Sukanik, C. N.; Ghabboun, J.; Cahen, D. J. *Am. Chem. Soc.* **2003**, *125*, 4730.
- Chernishova, I. V.; Hanumantha, R. *J. Phys. Chem. B* **2001**, *105*, 810.
- Vallant, T.; Kattner, J.; Brunner, H.; Mayer, U.; Hoffmann, H. *Langmuir* **1999**, *15*, 5339.
- Peters, R. D.; Nealey, P. F.; Crain, J. N.; Himpel, F. J. *Langmuir* **2002**, *18*, 1250.
- Tidswell, I. M.; Ocko, B.; Phershan, P. S.; Wasserman, S. R.; Whitesides, G. M.; Axe, J. D. *Phys. Rev. B* **1990**, *41*, 1111.
- Wyckoff, R. W. G. *Crystal Structures*, 2nd ed.; Interscience: New York, 1963–1971; Vol. 1, p 111.
- X-ray Data Base: JCPDS–IC 36–1451.